Dynamical quasicondensation in the weakly interacting Fermi-Hubbard model

Iva Březinová,[1,*] Markus Stimpfle,[1] Stefan Donsa,[1] and Angel Rubio[2,3]

[1]*Institute for Theoretical Physics, Vienna University of Technology, Wiedner Hauptstraße 8-10/136, 1040 Vienna, Austria, EU*

[2]*Max Planck Institute for the Structure and Dynamics of Matter, 22761 Hamburg, Germany, EU*

[3]*Center for Computational Quantum Physics (CCQ), Flatiron Institute, New York, New York 10010, USA*

(Received 20 February 2024; revised 22 April 2024; accepted 23 April 2024; published 15 May 2024)

We study dynamical (quasi)condensation in the Fermi-Hubbard model starting from a completely uncorrelated initial state of adjacent doubly occupied sites. We show that upon expansion of the system in one dimension, dynamical (quasi)condensation occurs not only for large interactions via the condensation of doublons, but also for small interactions. The behavior of the system is distinctly different in the two parameter regimes, underlining a different mechanism at work. We address the question of whether the dynamical (quasi)condensation effect persists in the thermodynamic limit. For this purpose, we use the time-dependent two-particle reduced density matrix method, which allows the extension to large system sizes, long propagation times, and two-dimensional (2D) systems. Our results indicate that the effect vanishes in the thermodynamic limit. However, especially in 2D, further investigation beyond numerically tractable system sizes calls for the use of quantum simulators, for which we show that the described effect can be investigated by probing density fluctuations.

DOI: 10.1103/PhysRevB.109.174308

I. INTRODUCTION

Superconductivity is one of the most intriguing collective electronic phenomena in solid state physics. The search for an explanation of high-temperature superconductivity in correlated materials still drives a considerable amount of experimental and theoretical work. Traditionally, superconductivity has been viewed as an effect of a system at (or near) equilibrium [1], but pioneering experiments (see, e.g., Refs. [2–10]) have shown that states with signatures of superconductivity can be induced by external driving. This has stimulated new interest in dynamical condensation effects in fermionic systems (see, e.g., Refs. [11–17]).

The workhorse for theoretical investigations of correlated phenomena in solid state physics is the Fermi-Hubbard model [18–22]. It has been shown analytically by Yang [23] that the Fermi-Hubbard model in arbitrary dimensions has a special symmetry, the so-called η symmetry, which gives rise to the appearance of a fermionic condensate in the excitation spectrum of the Fermi-Hubbard model. This so-called η condensate saturates the maximally allowed occupation number for pair states, whose value was also derived by Yang [24], and shows off-diagonal long range order [23]. Several recent theoretical works have been devoted to showing that ground states of the Fermi-Hubbard model can be driven to metastable nonequilibrium states with large overlap with the η condensate inheriting its properties (see, e.g., Refs. [12,13]).

Concomitantly, it was found in numerical studies [25,26] and subsequently measured experimentally [27] that initially uncorrelated states of hard-core bosons form a quasicondensate in one dimension (1D) upon free expansion. This effect has been explained through the physics of emergent Hamiltonians where the dynamical system inherits the properties of a ground state condensate of the emergent nonequilibrium Hamiltonian [28]. This study is highly relevant also for fermions since in the case of large interactions the fermions form pairs (doublons), which to a high degree of accuracy can be described as hard-core bosons. This mapping has been used to study dynamical quasicondensation of fermions in 1D at large interactions in, e.g., Refs. [14,29].

In this work we investigate dynamical (quasi)condensation upon a quench with similar initial conditions, but in the opposite limit of weak electron interactions $U < 1J$, where J is the hopping matrix element. We show that this dynamical (quasi)condensation effect exhibits a markedly different behavior than its counterpart at large U. We exploit our time-dependent two-particle reduced density matrix (TD2RDM) method [30–32] to reach the required long expansion times for system sizes of several tens of sites, while laying the ground based on small systems and exact calculations. We compare the results within the TD2RDM method with exact results for small systems to extrapolate its accuracy for larger systems where exact results are not available. Furthermore, the TD2RDM method allows one to extend the investigations to two-dimensional (2D) systems enabling us to address the question of whether the Mermin-Wagner-Hohenberg theorem [33,34], which prohibits any condensation in 1D in equilibrium in the thermodynamic limit, is also valid in this dynamical situation.

The paper is structured as follows. We introduce the system under investigation in Sec. II and review the essential building blocks of the TD2RDM method in Sec. III emphasizing necessary extensions to incorporate the η symmetry. We investigate dynamical (quasi)condensation in 1D in Sec. IV. We first discuss small systems that are treatable exactly. These small

*iva.brezinova@tuwien.ac.at

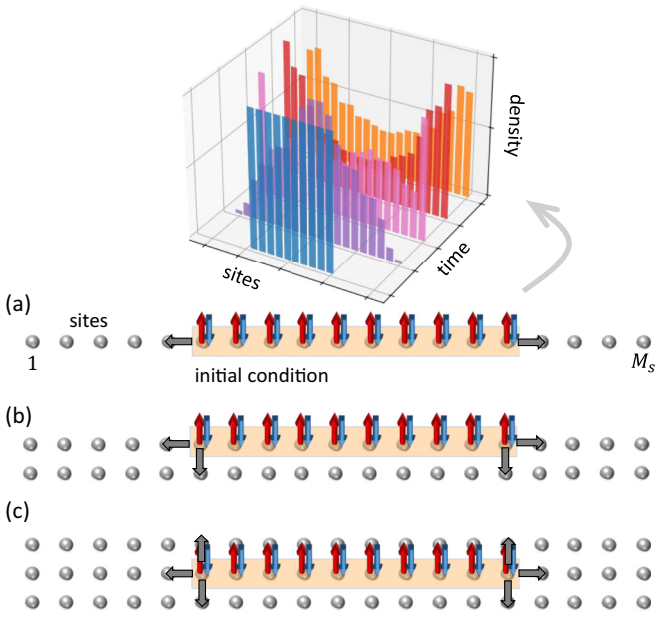

FIG. 1. Fermi-Hubbard model in (a) 1D and narrow strips in 2D with (b) two or (c) three transversal sites. The total number of sites is M_s. The orange bar represents the investigated initial condition of a block of adjacent doubly occupied sites either placed in the center (as shown in the images) or left aligned (not shown). The upper panel shows a few exemplary snapshots of the ensuing density fluctuations.

systems show already signatures of the effect and serve as benchmarks for the TD2RDM method. Extensions to substantially larger systems are performed within the TD2RDM method. In Sec. IV C we extend our research to 2D and conclude in Sec. V. As units we use $\hbar = m = e = 1$ unless otherwise stated.

II. OUT-OF-EQUILIBRIUM FERMI-HUBBARD MODEL

The system under investigation is the Fermi-Hubbard model in 1D and 2D (see Fig. 1) given by

$$\hat{H} = -J \sum_{\langle i,j \rangle} \sum_{\sigma} \hat{a}^{\dagger}_{i\sigma} \hat{a}_{j\sigma} + U \sum_{i} \hat{n}^{\uparrow}_{i} \hat{n}^{\downarrow}_{i}, \tag{1}$$

where $\langle i, j \rangle$ denotes nearest-neighbor hopping on a 1D or 2D lattice and $\hat{n}^{\uparrow(\downarrow)}_{i} = \hat{a}^{\dagger}_{i\uparrow(\downarrow)} \hat{a}_{i\uparrow(\downarrow)}$. The number of sites is M_s. As boundary conditions we use either periodic boundary conditions or hard-wall boundary conditions. In the case of hard-wall boundary conditions, the particle density is strictly zero at the entire boundary of the system, which extends beyond the sites plotted in Fig. 1. For example, in 1D, where the sites are enumerated from 1 to M_s, the hard-wall boundary is positioned at the sites 0 and $M_s + 1$.

In 1D we use half-filling, i.e., the number of particles N is given by $N = M_s$ and the number of spin-up and spin-down particles is equal. As initial states $|\Psi(0)\rangle$ we use $M_s/2$ adjacent doubly occupied sites, either centered in the middle of the system as shown in Fig. 1(a) or aligned to the left edge. Similar uncorrelated initial conditions have been used extensively as benchmarks for approximate methods to solve the time-dependent multiparticle Schrödinger equation; see, e.g., Refs. [35,36].

To explore the effect of dimensionality, we extend the 1D system by transversal degrees of freedom as depicted in Figs. 1(b) and 1(c). In this case the filling corresponds to $N = M_s/2$ in Fig. 1(b) and $N = M_s/3$ in Fig. 1(c) and the initial conditions used in these 2D cases are those depicted in the figure.

All these states are initially entirely uncorrelated, i.e., correspond to Hartree-Fock states. The correlation, however, strongly increases as a function of time as will be discussed in Sec. IV, which is key to the emergence of the (quasi)condensate. The initial states are highly excited, i.e., many states in the entire excitation spectrum have a non-negligible overlap. One might think that an ensuing dynamical (quasi)condensation effect requires a particularly large overlap with the η condensate $|\eta\rangle$, which is an exact excited eigenstate of the Hamiltonian Eq. (1). The overlap between our initial condition and the η condensate is, however, small as can be calculated analytically using the construction $|\eta\rangle = (\hat{\eta}^{+})^{N/2}|0\rangle$, where $|0\rangle$ is the vacuum state and

$$\hat{\eta}^{+} = \sum_{j} (-1)^{j} \hat{a}^{\dagger}_{j\downarrow} \hat{a}^{\dagger}_{j\uparrow}. \tag{2}$$

Using simple combinatorial arguments, we obtain in 1D in the case of half-filling, where $N = M_s$, that

$$|\langle \eta | \Psi(0) \rangle|^2 = \binom{M_s}{M_s/2}^{-1} \tag{3}$$

and remains so for $t > 0$. For large M_s, Eq. (3) goes like $\sim 2^{-M_s}$ and is thus exponentially suppressed. Therefore, although the dynamical (quasi)condensate described in this paper has the same energy expectation value and similar properties as the η condensate upon its dynamical formation, it cannot be explained by an actual proximity to it.

To investigate the dynamics of the system in the following, we solve the Schrödinger equation with the Hamiltonian Eq. (1) either by using exact diagonalization or by employing the TD2RDM method as discussed below.

III. TD2RDM METHOD AND η SYMMETRY

Within the TD2RDM method, we avoid the propagation of the wave function, and thus the problem of exponential scaling altogether, and instead resort to the propagation of the two-particle reduced density matrix (2RDM). The price we pay is a partial neglect of three-particle correlations, as briefly described in the following (for more details, see [30–32]).

The 2RDM is obtained from a wave function $|\Psi(t)\rangle$ by tracing out $N - 2$ particles as

$$D_{12}(t) = N(N-1)\mathrm{Tr}_{3\ldots N} |\Psi(t)\rangle\langle\Psi(t)|. \tag{4}$$

Similarly, the three-particle reduced density matrix (3RDM), required for the propagation of the equations of motion of the 2RDM, is given by

$$D_{123}(t) = N(N-1)(N-2)\mathrm{Tr}_{4\ldots N} |\Psi(t)\rangle\langle\Psi(t)| \tag{5}$$

and relates to the 2RDM via $D_{12} = 1/(N-2)\mathrm{Tr}_3 D_{123}$. For later reference we also introduce the one-particle reduced density matrix (1RDM) given by

$$D_1(t) = 1/(N-1)\mathrm{Tr}_2 D_{12} = N\mathrm{Tr}_{2\ldots N} |\Psi(t)\rangle\langle\Psi(t)|. \tag{6}$$

In a given single-particle basis the elements of $D_{12}(t)$ can be written as

$$D^{i_1\sigma_1' i_2\sigma_2'}_{j_1\sigma_1 j_2\sigma_2} = \langle\Psi(t)|\hat{a}^\dagger_{i_1\sigma_1'}\hat{a}^\dagger_{i_2\sigma_2'}\hat{a}_{j_2\sigma_2}\hat{a}_{j_1\sigma_1}|\Psi(t)\rangle. \tag{7}$$

We omit the numerical index (e.g., 12 for the 2RDM) whenever it is obvious from the number of indices in a specific single-particle basis which RDM we consider [as in Eq. (7)]. In the present case, a suitable basis corresponds to the individual sites of the Fermi-Hubbard model. In this basis, the uncorrelated initial conditions considered in this paper can be easily constructed as

$$D^{i\uparrow j\downarrow}_{i\uparrow j\downarrow} = 1 \tag{8}$$

for all doubly occupied sites i and j and zero otherwise. In the present case of a total spin singlet case it turns out that the construction of the entire D_{12} is not necessary because the spin block $D^{\uparrow\downarrow}_{12}$ contains all the information [30,32]. The equation of motion for this spin block within the Fermi-Hubbard model is then given by

$$\begin{aligned} i\partial_t D^{i_1\uparrow i_2\downarrow}_{j_1\uparrow j_2\downarrow} = &\sum_n h^{i_1}_n D^{n\uparrow i_2\downarrow}_{j_1\uparrow j_2\downarrow} + \sum_n h^{i_2}_n D^{i_1\uparrow n\downarrow}_{j_1\uparrow j_2\downarrow} + U\delta^{i_1,i_2} D^{i_1\uparrow i_2\downarrow}_{j_1\uparrow j_2\downarrow} \\ &- \sum_n h^n_{j_1} D^{i_1\uparrow i_2\downarrow}_{n\uparrow j_2\downarrow} - \sum_n h^n_{j_2} D^{i_1\uparrow i_2\downarrow}_{j_1\uparrow n\downarrow} \\ &- U\delta_{j_1,j_2} D^{i_1\uparrow i_2\downarrow}_{j_1\uparrow j_2\downarrow} + U D^{i_1\uparrow i_2\uparrow i_1\downarrow}_{i_1\uparrow j_2\uparrow j_1\downarrow} + U D^{i_1\uparrow i_2\uparrow i_2\downarrow}_{j_1\uparrow i_2\uparrow j_2\downarrow} \\ &- U D^{j_1\uparrow i_2\uparrow i_1\downarrow}_{j_1\uparrow j_2\uparrow j_1\downarrow} - U D^{i_1\uparrow j_2\uparrow i_2\downarrow}_{j_1\uparrow j_2\uparrow j_2\downarrow}, \end{aligned} \tag{9}$$

with

$$h^i_j = -J\delta^{i+1}_j - J\delta^{i-1}_j. \tag{10}$$

This equation scales like M_s^4 with the number of sites, which is key to the efficiency of the TD2RDM method. The closure of the equation of motion requires a reconstruction of the 3RDM via the 2RDM using an approximate stable reconstruction functional; for more details see [30–32] and Appendix A.

The η symmetry of the Hamiltonian leads to a further constant of motion that has to be considered, i.e., $[\hat{H}, \hat{\eta}^+\hat{\eta}^-] = [\hat{H}, \hat{\eta}_z] = 0$, with $\hat{\eta}^+$ given in Eq. (2), $\hat{\eta}^-$ being its Hermitian conjugate, and $\hat{\eta}_z = \frac{1}{2}\sum_j(\hat{n}_{j\uparrow} + \hat{n}_{j\downarrow} - 1)$ [23]. While the conservation of the expectation value of $\langle\hat{\eta}_z\rangle$ is guaranteed by the conservation of the particle number, the conservation of $\langle\hat{\eta}^+\hat{\eta}^-\rangle$ requires further scrutiny. Using the 2RDM, the expectation value $\langle\hat{\eta}^+\hat{\eta}^-\rangle$ can easily be calculated as

$$\langle\hat{\eta}^+\hat{\eta}^-\rangle = \sum_{i,j}(-1)^{i-j} D^{i\uparrow i\downarrow}_{j\uparrow j\downarrow} \tag{11}$$

and its behavior within the TD2RDM can be investigated by calculating its time derivative. The fact that the time derivative of Eq. (11) has to be zero, however, does not lead to further constraints on the 3RDM reconstruction functional as it requires only exchange symmetry. (This is in contrast to, e.g., the conservation of energy [35] which requires contraction consistency [30].) However, the TD2RDM suffers from the N-representability problem, which necessitates the application of purification [31,32,37,38]. We, therefore, have to adapt our purification procedure, which so far took only into account contraction consistency between the 2RDM and the 1RDM as well as energy conservation [32,38]. The modified purification procedure, which guarantees the conservation of all constants of motion including $\langle\hat{\eta}^+\hat{\eta}^-\rangle$, is described in Appendix B.

IV. DYNAMICAL (QUASI)CONDENSATION

Our figure of merit to assess the presence of a ferimionic (quasi)condensate is the largest eigenvalue of the 2RDM g_1 (i.e., the highest geminal occupation number) obtained from diagonalization of the 2RDM

$$D_{12}(t) = \sum_{j=1}^{r(r-1)/2} g_j(t)|g_j(t)\rangle\langle g_j(t)|, \tag{12}$$

where $|g_j(t)\rangle$ are the geminal states (pair states) and r is the number of single-particle basis states (orbitals). In our case $r = 2M_s$. In our convention, the geminal occupation numbers are ordered in descending order and g_1 is the largest occupation number. The geminal states can be grouped according to their spin symmetry into spin-singlet and spin-triplet states. In all cases reported below the largest geminal occupation number g_1 belongs to a spin-singlet state $|g_1\rangle$.

Yang showed [24] that g_j is bounded from above by

$$g_{\max} = \frac{N(r-N+2)}{r} \tag{13}$$

for a system of N fermions in r modes and with the normalization of the 2RDM as given in Eq. (4). Clearly, $g_{\max}$ is macroscopic, i.e., $O(N)$, showing that the smallest reduced density matrix allowing macroscopic occupations in fermionic systems is the 2RDM, in contrast to bosonic condensation, which manifests itself by a macroscopic occupation of an eigenstate of the 1RDM according to Penrose and Onsager [39]. The maximal geminal occupation number for bosonic systems thus scales as $O(N^2)$.

In case of half-filling, $N = r/2 = M_s$, we obtain

$$g_{\max} = \frac{N+2}{2}, \tag{14}$$

and for the other cases considered here, i.e., $N = r/4 = M_s/2$ and $N = r/6 = M_s/3$, we obtain $g_{\max} = (3N+2)/4$ and $g_{\max} = (5N+2)/6$, respectively.

When $g_{\max}$ is reached, all other $r(r-1)/2 - 1$ states have equal weight given by [40]

$$\bar{g} = \frac{2N(N-2)}{r(r-2)}. \tag{15}$$

It has been shown that states reaching $g_{\max}$ correspond to extreme antisymmetric geminal power (AGP) states [40], which can be constructed by antisymmetrization of a product ansatz of one pair state. The η condensate is an example for the realization of these states.

In the search for the dynamical (quasi)condensation we will monitor the time evolution of $g_1(t)$, whose proximity to $g_{\max}$ will signify the presence of a fermionic (quasi)condensate. When $g_1(t)$ approaches $g_{\max}$, all other eigenvalues should become close to equal. This behavior can be analyzed by means of a single quantity, i.e., the entropy of

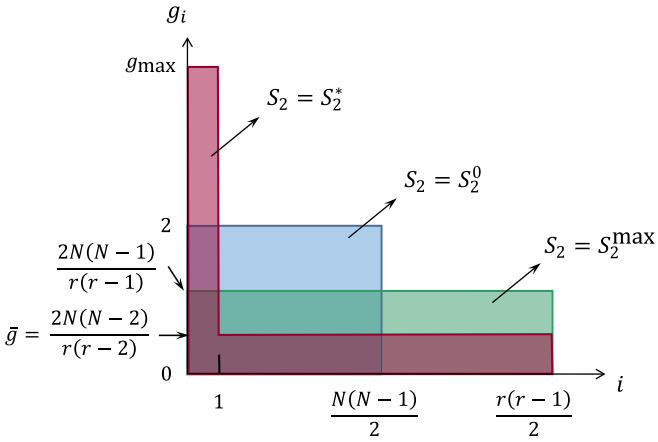

FIG. 2. Distribution of geminal occupation numbers for several distinct states. Blue: uncorrelated (Hartree-Fock) state with entropy S_2^0; red: extreme AGP state that reaches the predicted upper bound of $g_{\max}$ [Eq. (13)] and has an entropy of S_2^*; green: a state with the highest entropy $S_2^{\max}$ [Eq. (16)].

the distribution of geminal occupation numbers (see Fig. 2),

$$S_2(t) = -\sum_{i=1}^{r(r-1)/2} g_i(t) \ln g_i(t). \tag{16}$$

We evaluate S_2 by renormalizing $\sum_{i=1}^{r(r-1)/2} g_i = 1$. S_2 has been used as a measure of entanglement and correlations in the context of fermionic systems in, e.g., Refs. [41,42]. We denote the 2RDM entropy for an extreme AGP as S_2^*. Note that S_2^* is close to but not equal to the maximum $S_2^{\max}$ of S_2 given by an equal distribution of g_i; see Fig. 2.

A. Small systems in 1D

In this section, we want to provide a foundation for the study of large systems by discussing the essential features of the dynamical fermionic (quasi)condensation effect and benchmarking the TD2RDM method with exact results. This entails verifying whether the essential features of the effect are reproduced. We start our investigation with $M_s = 8$ sites and exact results. Tuning U from $U \ll 1J$ to $U \gg 1J$ we observe significant differences in the system's behavior; see Fig. 3. For $U = 4J$ and periodic boundary conditions, $g_1(t)$ fluctuates around $g_1(t) \approx 2$ as a function of time regardless of the position of the initial state [see Fig. 3(c) for the example of a left-aligned initial state]. The system thermalizes within $t \approx 5J^{-1}$, soon after the particle density completes a full circle around the system [Fig. 3(d)]. This behavior is also observed for a hard wall boundary and a centered initial condition, with thermalization occurring before any significant increase in $g_1(t)$.

Significantly different behavior is observed when employing a left-aligned initial state and hard wall boundary conditions. In this scenario, more space (i.e., half of the sites) is available for the system to expand freely until reaching the boundary. During this period, a noticeable enhancement of the pair-occupation number occurs, until g_1 reaches at the time $T_{\max}$ a maximum of about $g_1(T_{\max}) \approx 4$. Here and in the following, $T_{\max}$ represents the time of the first significant

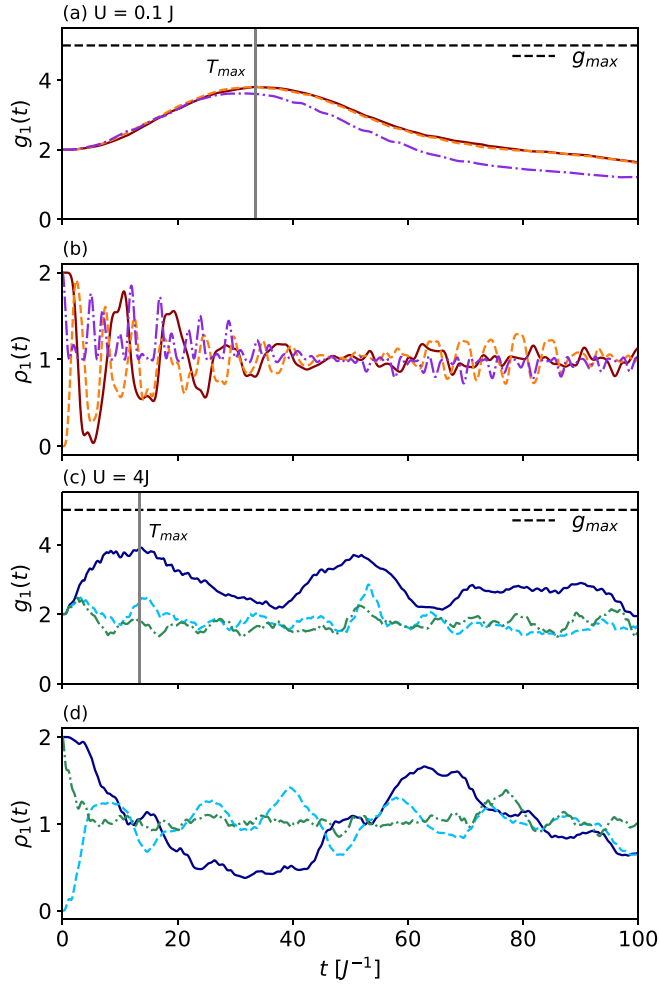

FIG. 3. Exact results for the $M_s = 8$ site Fermi-Hubbard model in 1D for different U, boundary conditions, and alignments of the initial state. (a), (b) $U = 0.1J$; (c), (d) $U = 4J$. Plotted is the maximal geminal occupation number as a function of time, $g_1(t)$, in (a) and (c), and the particle density at site one as a function of time, $\rho_1(t)$, in (b) and (d). In all subfigures solid lines correspond to hard wall boundary conditions and a left aligned initial state, dashed lines correspond to hard wall boundary conditions and a centered initial state [as in Fig. 1(a) for $M_s = 8$], and dashed-dotted lines correspond to periodic boundary conditions and a left aligned initial state.

maximum in $g_1(t)$ [see Fig. 3(c)]. Overall, the process of thermalization is slower, allowing for the observation of a second local maximum during the "back-and-forth" movement of the density; compare Figs. 3(c) and 3(d). These observations are in line with the physics of emergent Hamiltonians [28], elucidating the phenomenon of dynamical quasicondensation in the context of hard-core bosons upon free expansion [25]: the large interaction parameter U induces a pairing between the fermions, facilitating a mapping to hard-core bosons, also known as doublons (see, e.g., Ref. [14]). If the system can expand freely for a long enough time, quasicondensation emerges. However, the interaction with the boundary ultimately destroys the validity of the emergent Hamiltonian and with it the quasicondensate.

In our analysis of the dynamical (quasi)condensation effect, we focus on evaluating $T_{\max}$ and the associated

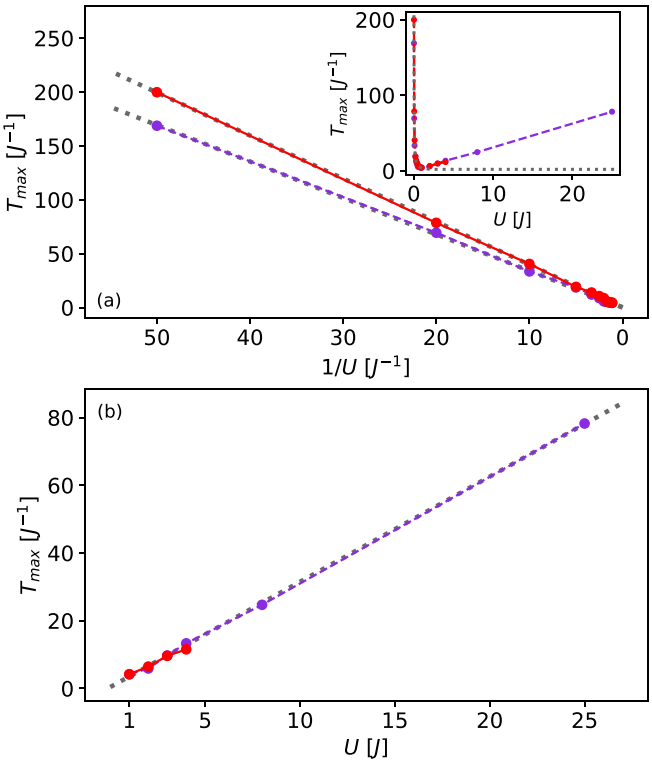

FIG. 4. Time of the first maximum in $g_1(t)$, $T_{\max}$ (see Fig. 3), as a function of U for the 1D Fermi-Hubbard model with $M_s = 8$, hard-wall boundary conditions, and a left aligned initial state. Solid lines are TD2RDM results; dashed lines correspond to exact results. The gray dotted lines represent linear fits. (a) Interval $U \in [0.02, 0.5]J$ with inverted axis; (b) $U \in [1, 25]J$. The inset in (a) shows the full U interval in linear scale. The gray dotted lines in each figure correspond to linear fits and to a $1/U$ fit in the inset.

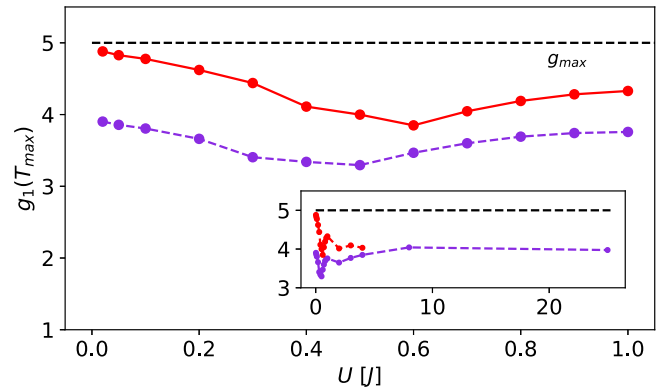

FIG. 5. Maximal value of the largest occupied geminal at $T_{\max}$, $g_1(T_{\max})$, for different U for the 1D Fermi-Hubbard model with $M_s = 8$, hard-wall boundary conditions, and a left aligned initial state. Solid lines are TD2RDM results; dashed lines correspond to exact results. The black dashed horizontal line marks the maximal possible two-state occupation number $g_{\max} = 5$ for $M_s = 8$. The inset shows the full analyzed U interval (the exact results extend towards larger values).

amplitude of the geminal occupation number $g_1(T_{\max})$. For $U \geqslant 1J$ we observe that $T_{\max}$ scales linearly with U, i.e., $T_{\max} \propto U$ [Fig. 4(b)]. This behavior can be attributed to the rescaled hopping matrix element of the doublons, which is proportional to J^2/U (see, e.g., Ref. [14]). The dynamical (quasi)condensation effect is least pronounced [i.e., $g_1(T_{\max})$ is smallest] in the range of $U \approx 0.6J$, i.e., at values slightly smaller compared to $U = 1J$, for which we observe the transition in the behavior of $T_{\max}$. At $U \approx 0.6J$, the amplitude is $g_1(T_{\max}) \approx 3.5$ (Fig. 5). As U increases, $g_1(T_{\max})$ nonmonotonically increases, reaching saturation at $g_1(T_{\max}) \approx 4$. To extract $T_{\max}$ and $g_1(T_{\max})$ for $U \geqslant 2J$ both in the exact results as well as in the TD2RDM results below, we have averaged $g_1(t)$ over small intervals of $\Delta t = 2.5J^{-1}$ to eliminate the effect of the high frequency fluctuations visible, e.g., in Fig. 3(c). Small local peaks around the overall maximum would influence the position of $T_{\max}$ otherwise.

For small $U < 1J$, the behavior of the system is strikingly different. We observe the emergence of a broad maximum, with $g_1(t)$ approaching $g_{\max}$ independent of the initial state's position and the chosen boundary conditions [Fig. 3(a)]. The specific quantitative value of $T_{\max}$ is unaffected by the initial state's position and exhibits only a mild dependence on the selected boundary conditions. Notably, the particle density undergoes multiple fluctuations between the systems' boundaries during the development of the broad maximum in $g_1(t)$, without thermalizing the system. This observation leads us to the conclusion that this phenomenon represents a dynamical (quasi)condensation effect, distinct from those captured by an emergent Hamiltonian. We present a detailed analysis that further supports this statement in Appendix C, where we show that the Hamiltonian Eq. (1) for $U < 1$ does not lead to an emergent time-dependent Hamiltonian that is (approximately) conserved during time evolution as required by [28].

Accordingly, in contrast to the linear scaling with U for $U > 1J$, we observe an inverse scaling behavior of $T_{\max}$ for $U < 1J$, i.e., $T_{\max} \propto 1/U$; see Fig. 4(a). $g_1(T_{\max})$, in turn, increases with decreasing U reaching again values close to $g_1(T_{\max}) \approx 4$.

We now proceed to analyze whether these observations are captured by our approximate TD2RDM method, as an underpinning for our studies of larger systems, where the effect is more pronounced. For $U > 1J$ we observe that the TD2RDM method is in very good agreement with the exact results, accurately predicting the linear dependence of $T_{\max}$ on U and the slope. The small discrepancy for $U = 4J$ originates from a local fluctuation around the global maximum present even after averaging within TD2RDM but not present in the exact result; compare Figs. 6(c) and 6(d). For $U < 1J$ the TD2RDM method correctly predicts the $1/U$ behavior but slightly overestimates the proportionality constant. Simultaneously, $g_1(T_{\max})$ is overestimated but the overall behavior is again captured very well; see Fig. 5. The most notable discrepancy is the prediction of the minimum of $g_1(T_{\max})$ as a function of U at $U \approx 0.5J$ compared to the exact results, which predict the minimum to be at $U \approx 0.6J$.

To gain a deeper understanding of these discrepancies, we further scrutinize the dynamics of all geminal occupation numbers as predicted by the approximate TD2RDM method and compare them to the exact results. We observe that as $g_1(t)$ evolves towards its maximum, all other geminal

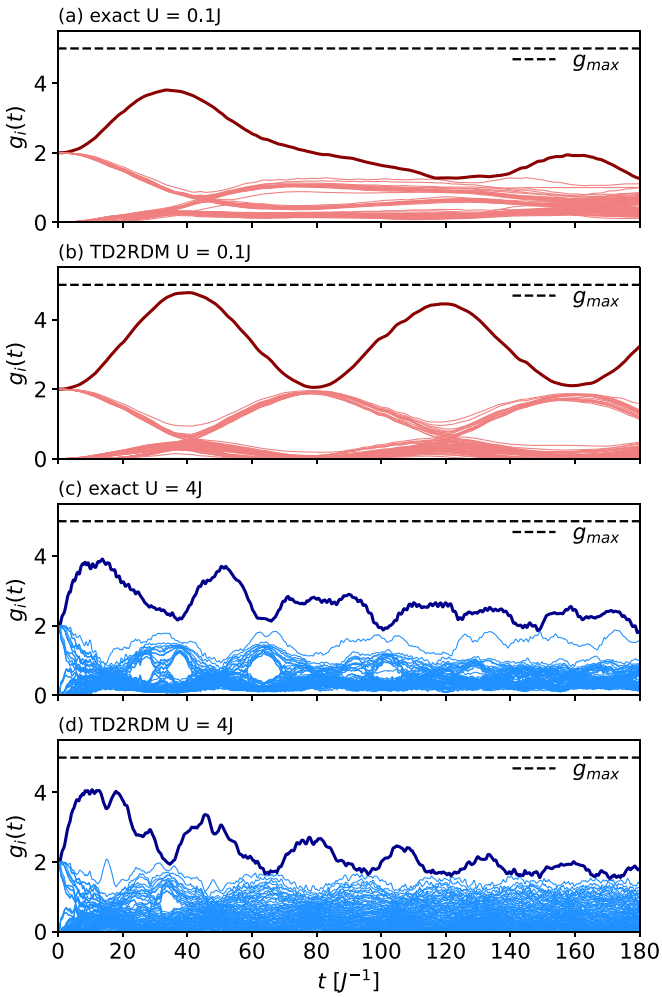

FIG. 6. Comparison between exact and TD2RDM results for the dynamics of all geminal occupations numbers $g_i(t)$ for the 1D Fermi-Hubbard model with $M_s = 8$, hard-wall boundary conditions, and a left aligned initial state. The largest geminal occupation number $g_1(t)$ is drawn with a thicker line and darker color. (a) Exact results for $U = 0.1J$, (b) TD2RDM results for $U = 0.1J$, (c) exact results for $U = 4J$, and (d) TD2RDM results for $U = 4J$.

occupation numbers approach each other, consistent with the expectation that, when $g_{\max}$ is reached, all other geminals are occupied by $\bar{g}$, Eq. (15) [see Fig. 6(a)]. However, the exact results show a small time shift between the maximum of $g_1(t)$ and the time at which all other $g_{i>1}(t)$ are closest. This leads to $g_1(T_{\max})$ being noticeably smaller than $g_{\max}$. Furthermore, the exact results show a small revival of the maximum at $t \approx 160J^{-1}$. In contrast, the TD2RDM results lack this shift, resulting in an overestimation of the amplitude $g_1(T_{\max})$. Additionally, the TD2RDM results exhibit prominent periodic revivals, indicating that relaxation effects are underestimated. Notably, the TD2RDM prediction for $U = 4J$ is remarkably accurate, even capturing the third revival of $g_1(t)$. The fact that the TD2RDM predicts the effect for $U > 1J$ more accurately than for $U < 1J$ is most likely an effect of time scales. While for $U > 1J$ the density fluctuations and the buildup of $g_1(t)$ occur on comparable time scales, for $U < 1J$ the density fluctuates much faster, i.e., many times back and forth, on the time scale of $T_{\max}$. Relative to the characteristic time scale of the density fluctuations, the system has to evolve much longer in the case of $U < 1J$ for the buildup of $g_1(t)$ than in the case of $U > 1J$.

We focus in our further analysis on the scaling behavior of $T_{\max}$ and $g_1(T_{\max})$, which is overall very well captured by the TD2RDM method; see Figs. 4 and 5. We would like to point out that our previous results [32] indicate that the TD2RDM method is more accurate for larger systems with $M_s \gtrsim 20$ than for systems as small as $M_s = 8$. While for $M_s = 8$ the TD2RDM method overestimates the density fluctuations for $t > 60J^{-1}$ (not shown) consistent with the deviations obtained for the geminal occupation numbers, we have observed almost perfect agreement for the density fluctuations in the case of $M_s = 18$ in [32]. The predictions for $T_{\max}$ and the amplitude $g_1(T_{\max})$ within TD2RDM may, therefore, be even more accurate than a straightforward extrapolation of the results for $M_s = 8$ allows one to judge.

B. Larger systems in 1D

We now turn to the fundamental question of whether the observed effect exhibits characteristics of a quasicondensate that vanishes in the thermodynamic limit or whether this dynamical setting enables a circumvention of the Mermin-Wagner-Hohenberg theorem which prohibits condensation in 1D in equilibrium [34]. To address this question, we explore using the TD2RDM method significantly larger system sizes for which there are no exact benchmarks available, bearing in mind that the TD2RDM might slightly overestimate both $T_{\max}$ as well as $g_{\max}$, while maintaining a reliable prediction of the overall behavior and scaling.

We start our investigation with a system of $M_s = 20$ for which we make a detailed comparison to the system with $M_s = 8$. Figure 7 shows one particular example of the behavior for $M_s = 20$. Similar to the case of $M_s = 8$, the largest geminal occupation number $g_1(t)$ rises to a pronounced maximum of $g_1(T_{\max}) \approx 10$ close to $g_{\max} = 11$ and several revivals appear [Fig. 7(a)]. These strong revivals are again most likely spurious.

It is instructive to explore in parallel the density fluctuations of the system [Fig. 7(c)]. We observe strong fluctuations in between the boundaries of the system and several reflections from the hard walls except for a short interval in time around $T_{\max}$, where the particle density becomes homogeneous. This effect is accompanied by a local maximum in the single-particle entropy S_1 obtained from the diagonalization of the 1RDM [Eq. (6)],

$$D_1(t) = \sum_{j=1}^{r} n_j(t) |n_j(t)\rangle \langle n_j(t)|, \tag{17}$$

given by

$$S_1(t) = -\sum_{j=1}^{r} n_j(t) \ln n_j(t). \tag{18}$$

We have again renormalized $\sum_{i=1}^{r} n_i = 1$ to calculate the entropy S_1. The maximum at $T_{\max}$ is given by $S_1(T_{\max}) = 3.68$, which is very close to the maximal value of $S_1^{\max} = 3.69$ for equally distributed natural occupation numbers for

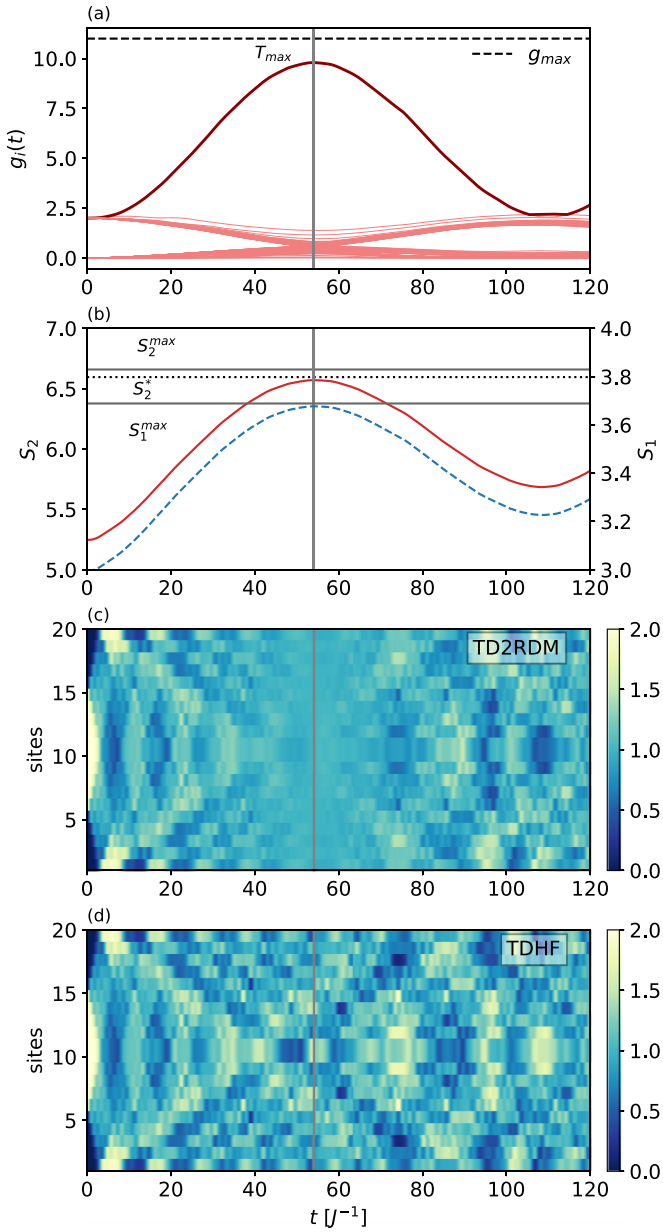

FIG. 7. TD2RDM results for the Fermi-Hubbard model in 1D with $M_s = 20$, $U = 0.1J$, hard-wall boundary conditions, and a centered initial condition. (a) Geminal occupation numbers, (b) entropies S_2 (left y axis) and S_1 (dashed line, right y axis), and particle-density fluctuations as a function of time within (c) TD2RDM and (d) TDHF. The vertical lines mark the time $T_{\max}$. In (b) the upper solid horizontal line corresponds to $S_2^{\max}$, the lower corresponds to $S_1^{\max}$, and the dotted horizontal line corresponds to S_2^*.

$r = 2M_s = 40$ [see Fig. 7(b)]. Overall, $S_1(t)$ follows the curve of the two-particle entropy $S_2(t)$, Eq. (16).

The homogeneous distribution of the particle density over the entire system follows from the fact that an extreme AGP state belongs to one of the quantum many-body states that maximize S_1, and is a direct consequence of the fact that the observed state is close to an extreme AGP state, with natural orbitals distributed over the entire system and their occupation numbers being almost equal.

It is instructive at this point to compare the density fluctuations to time-dependent Hartree-Fock (TDHF) calculations. Since U is relatively small, TDHF is able to predict the density fluctuations with remarkable accuracy up until the time near $T_{\max}$, where it completely fails to predict that the density becomes homogeneous; see Fig. 7(d). Interestingly, the revived density fluctuations for $t > T_{\max}$ are again very similar to the prediction of the TD2RDM method but exhibit a π-phase shift (i.e., the maxima coincide with the minima in the density and vice versa). These observations are also interesting from the point of view of the Hubbard-Stratonovich transformation [43,44], with which it is possible to transform the term quartic in the creation and annihiliation operators in the time-evolution operator into a quadratic term, at the expense of a new classical field to which the now noninteracting fermions couple. In other words, the interacting fermionic system is transformed into a noninteracting system whose dynamics is governed by an additional classical field. The often used stationary phase approximation of the Hubbard-Stratonovich transformation leads to the equations of motion of TDHF with the classical field being the TDHF mean field [45]. It is interesting to see that the noninteracting fermions moving in the mean field of the TDHF approximation reproduce the density fluctuations well until they fail to condense close to $T_{\max}$. These observations will guide our future studies to gain a more intuitive understanding of the effect.

The striking effect of the particle density becoming homogeneous during a small but finite time interval ΔT around $T_{\max}$ opens the door for an experimental study of these effects within the platforms of ultracold quantum simulators. While the increase of the pair-state occupation number is not easily accessible experimentally, the monitoring of the density fluctuations of the system has become an experimental routine on these platforms (see, e.g., Refs. [46–50] for a current experimental realization of a 1D periodic system, see [51]) and would allow one to measure $T_{\max}$ for even larger systems and other geometries. ΔT depends on the width of the maximum in $g_1(t)$, which increases with $T_{\max}$, i.e., with $1/U$ [see Fig. 8(a)]. In Fig. 8(a) we plot ΔT exemplary for hard wall boundary conditions by determining the time interval for which the weight of the Fourier components with $k > 0$ for the density fluctuations in Fig. 7(c) fall below a certain limit showing its approximate $1/U$ dependence.

When considering different boundary conditions and positions of the initial state, we observe again only a weak dependence of the dynamical (quasi)condensation effect on them. $T_{\max}$ as a function of U is practically equal for both boundary conditions; see Fig. 8(a). $g_1(T_{\max})$ behaves similarly for the two different boundary conditions but overall the decay with U is slower in the case of periodic boundary conditions and less monotonic. A further analysis of the state $|g_1(T_{\max})\rangle$ reveals another interesting consequence of the boundary conditions. When comparing the state $|g_1(T_{\max})\rangle$ to the η condensate in momentum space we observe for periodic boundary conditions that $|g_1(T_{\max})\rangle$ shows the typical η pairing of k and $k - \pi$ for particles of different spin; see Fig. 9. $|g_1(T_{\max})\rangle$ shows only small deviations from the η condensate [see Fig. 9(c)] – most notably a larger spread and a local minimum across the $k_2 = \pi - k_1$ lines in momentum space [Fig. 9(a)]. In contrast, for the system with hard-wall

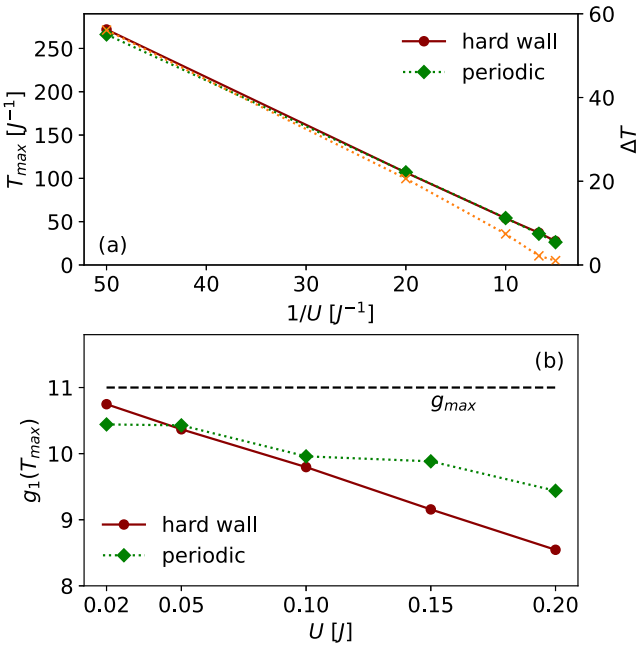

FIG. 8. (a) $T_{\max}$ and (b) the amplitude of the maximum of the largest geminal occupation number $g_1(T_{\max})$ as a function of U for $M_s = 20$ sites and different boundary conditions. In (a) on the second y axis we plot with crosses exemplary for hard wall boundary conditions ΔT (i.e., the width of the time window, where the density fluctuations become homogeneous).

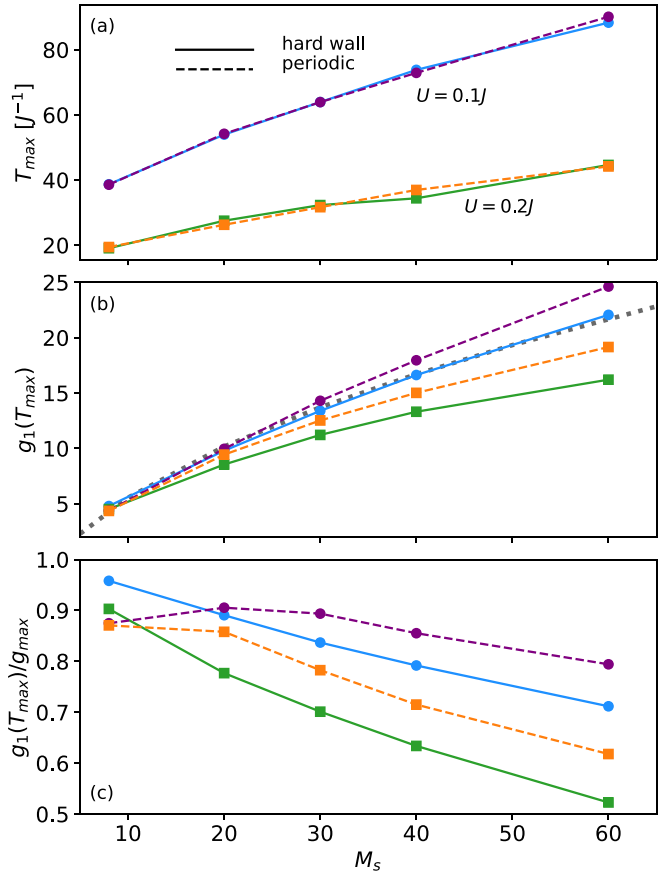

FIG. 10. Dynamical quasicondensation as functions of system size M_s. (a) $T_{\max}$, (b) $g_1(T_{\max})$, and (c) $g_1(T_{\max})$ relative to the maximum $g_{\max}$ [Eq. (13)] for hard-wall boundary conditions (solid), periodic boundary conditions (dashed), $U = 0.1J$ (dots), and $U = 0.2J$ (squares). The gray dotted line in (b) corresponds to a fit to a square root function.

boundary conditions, the reflections at the boundaries lead to the emergence of additional pairings, most notably Cooper-pair-like pairs with $k_1 = -k_2$; see Fig. 9(b). The Cooper-pair-like pairing becomes less pronounced for larger systems because, during the buildup of $g_1(t)$ up until its maximum at $T_{\max}$, the fluctuating density interacts less times with the hard-wall boundary. Note that the absolute square of the momentum distribution for the η state is equal for periodic and hard-wall boundary conditions. Despite these differences in the properties of the (quasi)condensate state, the geminal occupation numbers show similar behavior for both boundary conditions (Fig. 8).

We now turn to analyzing the behavior of the (quasi)condensation effect with system size. Since parameter scans are numerically increasingly demanding with system size we focus on two parameters for the on-site interaction, i.e., $U = 0.1J$ and $U = 0.2J$. We observe for both values of U that $T_{\max}$ increases with M_s in a nonlinear way [Fig. 10(a)]. The influence of the boundary conditions is negligible. In agreement with the previous investigations for $M_s = 8$, we observe that $T_{\max}$ is larger for $U = 0.1J$ than for $U = 0.2J$ for all investigated M_s. The amplitude of the first maximum $g_1(T_{\max})$ increases monotonically with M_s [Fig. 10(b)]. Most importantly, in the given available interval, the increase is proportional to $\sqrt{M_s}$. Consequently, we observe a monotonic

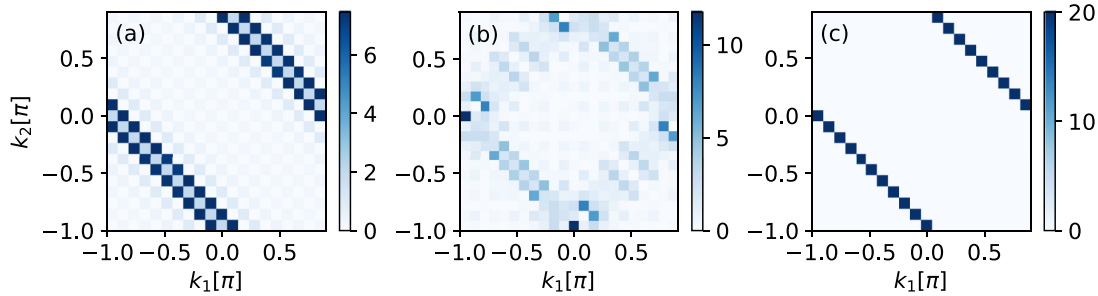

FIG. 9. Absolute square of the momentum distribution of the state $|g_1(T_{\max})\rangle$ for $M_s = 20, U = 0.1J$, (a) periodic boundary conditions, and (b) hard-wall boundary conditions. (c) Absolute square of the momentum distribution of the η condensate for $M_s = 20$ and periodic boundary conditions.

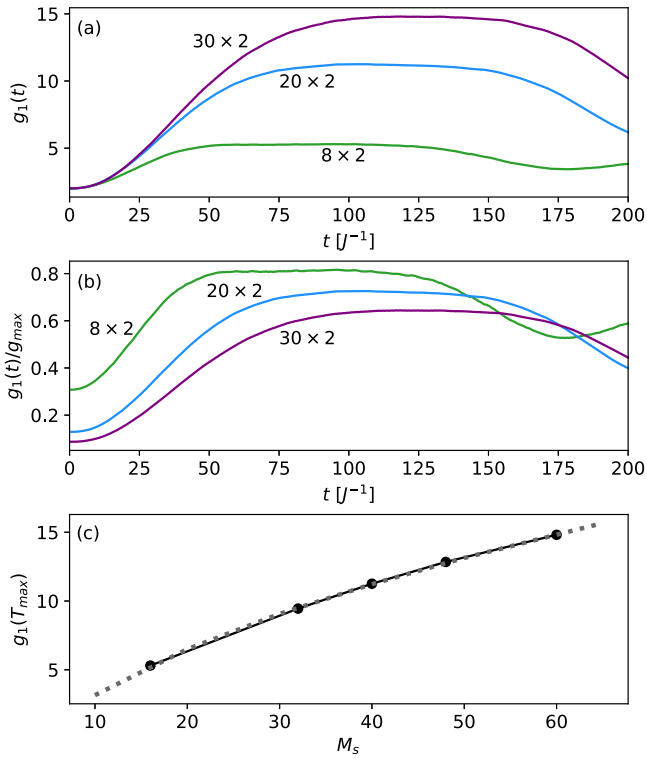

FIG. 11. (a) Largest geminal occupation number $g_1(t)$ and (b) $g_1(t)$ relative to $g_{\max}$ as a function of time for $U = 0.1J$ for different 2D stripe geometries with $M_s = 8 \times 2$ and $N = 8$, $M_s = 20 \times 2$ and $N = 20$, and $M_s = 30 \times 2$ and $N = 30$. (c) The largest value $g_1(T_{\max})$ as a function of the number of sites M_s for the systems in (a). The gray dashed line represents a fit to a square root function of M_s.

decrease of $g_1(T_{\max})$ with respect to $g_{\max}$. Since $g_{\max}$ grows linearly with M_s [Eq. (13)] our results indicate that $g_1(T_{\max})/g_{\max} \propto 1/\sqrt{M_s}$ in the thermodynamic limit. In other words, if the $\sqrt{M_s}$ dependence of $g_1(T_{\max})$ is preserved in the thermodynamic limit of $M_s \to \infty$, then in the thermodynamic limit $g_1(T_{\max})/g_{\max} \to 0$. Our results thus predict that the observed effect is a dynamical quasicondensate.

In the following section, we will investigate whether we might obtain a true condensation in 2D, i.e., in the presence of transverse degrees of motion, by extending the system to narrow 2D stripes.

C. Extension to 2D systems

We restrict our study here to hard-wall boundary conditions as these are more easily realizable experimentally in 2D systems. The geometries we investigate here are depicted in Figs. 1(b) and 1(c). For these systems with large M_s systematic scans with U and M_s are increasingly expensive even within the TD2RDM method such that we focus here on the question of whether we get an indication of a convergence to finite values of $g_1(T_{\max})/g_{\max}$ in the thermodynamic limit. For this purpose we stick to $U = 0.1J$ and $U = 0.2J$ for different geometries and numbers of sites M_s.

When extending the 1D system by one transversal site along the entire length as in Fig. 1(b) we observe a buildup

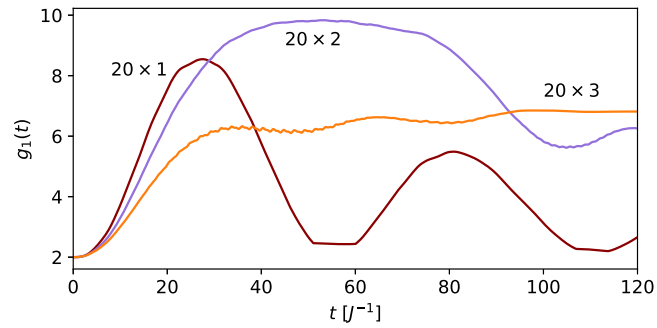

FIG. 12. Largest geminal occupation number $g_1(t)$ as a function of time for $U = 0.2J$ and number of particles $N = 20$ and different stripe geometries with $M_s = 20 \times 1$ (1D), $M_s = 20 \times 2$, and $M_s = 20 \times 3$ sites amounting to different fillings.

of a maximum in $g_1(t)$ over time; see Fig. 11(a) for different M_s and a filling of 1/4 (i.e., $N = M_s/2 = r/4$) and Fig. 11(b) for $g_1(t)$ relative to $g_{\max}$. In this case, the prediction for $g_{\max}$ [Eq. (13)] is equal to $g_{\max} = (3N + 2)/4$, i.e., larger than in the case of half-filling, Eq. (14). It is striking that the maxima are much broader than in 1D extending over longer periods of time. For $g_1(T_{\max})$ we observe a sublinear (square root) increase with M_s [Fig. 11(c)], while convergence of $g_1(T_{\max})/g_{\max}$ towards finite values would require a linear increase. The conclusion from these results is thus that the condensation effect will vanish in the thermodynamic limit.

Increasing the system further by another transverse degree of freedom as in Fig. 1 changes the picture quite strongly; see Fig. 12. For the system with $M_s = 20 \times 3$ sites we observe a fast increase in $g_1(t)$ initially but then a flattening and a further increase at a much smaller pace. Until a time of around $t = 100J^{-1}$, which is already numerically quite costly, the largest geminal occupation number g_1 does not come close to $g_{\max} = (5N + 2)/6 = 17$ for this case of sixth filling. It is difficult to estimate based on these observations whether the system develops a (quasi)condensate at some later point in time, but the curves obtained so far indicate that the effect does not persist in 2D.

V. CONCLUSIONS

We have numerically investigated dynamical quasicondensation in the Fermi-Hubbard model starting from a completely uncorrelated initial state of adjacent doubly occupied sites. In 1D we have shown that upon expansion of the system the largest eigenvalue of the two-particle reduced density matrix (2RDM), $g_1(t)$, develops a local maximum that comes close to the theoretical upper limit $g_{\max}$ predicted by Yang [24], signaling the appearance of fermionic pair condensation. This dynamical quasicondensation is accompanied by strong two-particle correlations as measured by the two-particle cumulant and the two-particle entropy obtained from the eigenstates of the 2RDM. This condensation effect appears for all investigated values of the interaction U, but shows a distinctly different behavior for small $U < 1J$ as compared to large $U > 1J$, where J is the hopping matrix element. In the case of $U > 1J$, the quasicondensation effect has been explained by the physics of an emergent Hamiltonian [28] and requires

a completely free expansion. In contrast, for small $U < 1J$ we observe that the system undergoes many interactions with the boundaries of the system on the characteristic time scale $T_{\max}$ during which the dynamical quasicondensate emerges. The effect is only weakly dependent on whether we chose hard-wall or periodic boundary conditions. Interestingly, the two-particle quasicondensate state does dependent on the boundary conditions and features the typical η-condensate pairing in case of periodic boundary conditions and both an η-condensate pairing, and a Cooper-pair-like pairing in case of hard-wall boundary conditions for small enough systems that interact with the boundary sufficiently many times. Moreover, the scaling of both $T_{\max}$ and the amplitude $g_1(T_{\max})$ with U is markedly different for $U < 1J$ and $U > 1J$. For $U < 1J$ we observe that $T_{\max} \propto 1/U$, while for $U > 1J$ one obtains $T_{\max} \propto U$.

It is so far an open question of whether it is possible to circumvent the Mermin-Wagner-Hohenberg theorem [33,34] in a dynamical setting. The Mermin-Wagner-Hohenber theorem prohibits the appearance of condensation in 1D in the thermodynamic limit in equilibrium. We address this question for our weakly interacting quasicondensation effect by expanding to system sizes of up to 60 sites. To propagate these systems over the required long periods of time we employ our time-dependent 2RDM (TD2RDM) method. Based on comparisons with exact results for small system sizes we have demonstrated that the TD2RDM method accurately predicts the essential features of the effect such that extrapolation to large systems, where exact benchmarks do not exist, can be made. The analysis of the effect with increasing system size reveals that the maximum of g_1 grows proportionally to the square root of the system size while $g_{\max}$ grows linearly. Our results thus indicate that $g_1(T_{\max})/g_{\max}$ vanishes in the thermodynamic limit, a defining feature of a quasicondensate.

To further expand on this question, we have extended our system to narrow 2D stripes allowing for transversal motion during expansion. For systems with two transverse sites, we observe broad maxima in g_1 over longer periods of time compared to the 1D case. The scaling of $g_1(T_{\max})$ with the system size, however, again indicates a vanishing condensation effect in the thermodynamic limit. A further increase, of the transverse degrees of freedom seems to lead to a strong deterioration of the effect. In this case, g_1 increases strongly initially but then flattens, featuring a slow but steady increase over the entire investigated time interval during which, however, g_1 does not come as close to $g_{\max}$ as in the previous cases. Further increase in the number of transversal degrees of freedom to approach a sufficiently large square lattice is planned in the future.

Our results open the door to further scrutinize this effect in the platform of experimental quantum simulators with single-site resolution [46–50], where substantially larger system sizes both in 1D and 2D could be probed. We have shown that the appearance of the quasicondensation effect is accompanied with spatial particle density fluctuations becoming homogeneous over the entire system for a short but finite period of time around $T_{\max}$. Strong density fluctuations reappear shortly after $T_{\max}$. This effect can be traced back to the single-particle entropy obtained from the eigenvalues of the one-particle reduced density matrix showing a local maximum. Since probing the particle density distribution is an experimental routine nowadays, observing a homogeneous density over finite periods of time could serve as a strong indication of the dynamical (quasi)condensation effect.

Our results highlight the potential of the TD2RDM method to deliver predictions for system sizes and time scales not reachable by any other method. We would like to point out that our present code, while exploiting several symmetries of the system, is not fully optimized and heavily parallelized yet. Further improvement of its optimization and employing multinode parallelization should allow one to compute the dynamics in systems with a number of sites of about a factor of 2 larger than the largest systems in the present study over similar time scales. With this extension, investigations of condensation effects on a square lattice in 2D should become possible. The TD2RDM method could thus provide benchmarks and guidance for studies on nonequilibrium systems on quantum simulators for large systems.

The observed effect may also be relevant to 2D materials. Vertical stacking of two identical layers with a small twist angle between them yields moiré superstructures with quite large periodicity angles, exceeding 10 nm. For the case of, e.g., twisted bilayer graphene, the low-energy electronic structure of the resulting moiré systems features moiré flat bands resulting in a plethora of many-body phenomena such as superconductivity or correlated insulator states [52]. The density is concentrated around the AA sites of the moiré, which form a triangular lattice with a lattice constant of $\approx$15 nm, tunable by the twist angle. Over such distances, it should be possible to create sufficiently strong static electric fields through the application of gate voltages to create initial conditions close to those studied in the present paper. Another interesting question that might arise in 2D systems is the condensation of excitons, to which the 2RDM provides direct access (see, e.g., Ref. [53]). The extension of our method to realistic systems would require to take into account both finite temperature and interactions with phonons. We plan to incorporate these effects and apply our method to 2D materials in future studies.

ACKNOWLEDGMENTS

We thank Marie Eder, Salvatore R. Manmana, Florian Libisch, and Joseph Tindall for helpful discussions and hints on literature. I.B. thanks the Simons Foundation for the great hospitality and support during her research visit at the CCQ of the Flatiron Institute, where parts of this research were conducted. The Flatiron Institute is a division of the Simons Foundation. We acknowledge support from the Max Planck–New York City Center for Non-Equilibrium Quantum Phenomena, Cluster of Excellence 'CUI: Advanced Imaging of Matter'–EXC 2056–project ID. This research was funded by the Austrian Science Fund (FWF) Grant No. P 35539-N, as well as by the FWF Grant No. 10.55776/COE1. Calculations were performed on the Vienna Scientific Cluster (VSC4).

APPENDIX A: RECONSTRUCTION WITHIN THE TD2RDM METHOD

Our reconstruction functionals are based on the cumulant expansion of the 3RDM [54]

$$D_{123} = \hat{A}D_1D_2D_3 + \hat{A}\Delta_{12}D_3 + \Delta_{123}, \tag{A1}$$

which represents a separation into elements with different levels of particle correlations. $\hat{A}$ is an antisymmetrization operator that creates only permutations that give nonequivalent terms,

$$\Delta_{12} = D_{12} - \hat{A}D_1D_2 \tag{A2}$$

is the two-particle cumulant representing two-particle correlations, and Δ_{123} is the three-particle cumulant. Using the cumulant expansion, an approximate reconstruction functional of D_{123} boils down to finding physically motivated reconstruction functionals for the three-particle cumulant Δ_{123}. We have shown previously that a stable and accurate propagation of Eq. (9) requires that the reconstructed 3RDM correctly contracts into the two-particle space [30]. Only then are conservation of energy and spin symmetries guaranteed at all times during time propagation. This contraction consistency [30] can be achieved employing the unitary decomposition (see, e.g., Refs. [37,55,56]), which allows one to decompose a tensor into its trace-free kernel and the orthogonal component (with respect to the Hilbert-Schmidt inner product), which carries traces. The orthogonal component is an exact functional of the traces of the tensor and can thus be easily determined. We employ here the reconstruction functional by Valdemoro and co-workers [57] and enforce construction consistency [30,32]. Enforcing contraction consistency leads to a scaling with M_s^5. Due to the linearity of the unitary decomposition, this reconstruction of the 3RDM amounts to neglecting the kernel (i.e., the trace free component) of Δ_{123} in Eq. (A1). We do not use the Nakatsuji-Yasuda reconstruction [32,58] of the three-particle cumulant here because the buildup of the (quasi)condensate leads to a large two-particle cumulant as a function of time without concomitant increases in the three-particle cumulant such that the Nakatsuji-Yasuda reconstruction, while being initially more accurate, leads to overall larger reconstruction errors as time progresses.

The dynamics of the two-particle cumulant can be used as an accurate measure of the quality of the TD2RDM method. For the small system with $M_s = 8$ sites from Sec. IV A we gain further insights into the approximations entailed within the TD2RDM method. Evaluating the Frobenius norms of the two-particle cumulants for spin-polarized pairs, $|\Delta_{12}^{\uparrow\uparrow}|_2$, and spin-unpolarized pairs, $|\Delta_{12}^{\uparrow\downarrow}|_2$, as a measure for two-particle correlations reveals that the TD2RDM overestimates the pairing of spin-unpolarized pairs while underestimating the production of spin-polarized pairs; see Figs. 13(a) and 13(b). This analysis can be complemented by means of the entropy $S_2(t)$, which concentrates the information on all geminal occupation numbers into one quantity. We observe that $S_2(t)$ increases as a function of time, reaching S_2^* for an extreme AGP state at a time close to $T_{\max}$ [Fig. 13(c)]. The TD2RDM results closely follow the exact results initially, but then $S_2(t)$ remains large within the exact results while spuriously

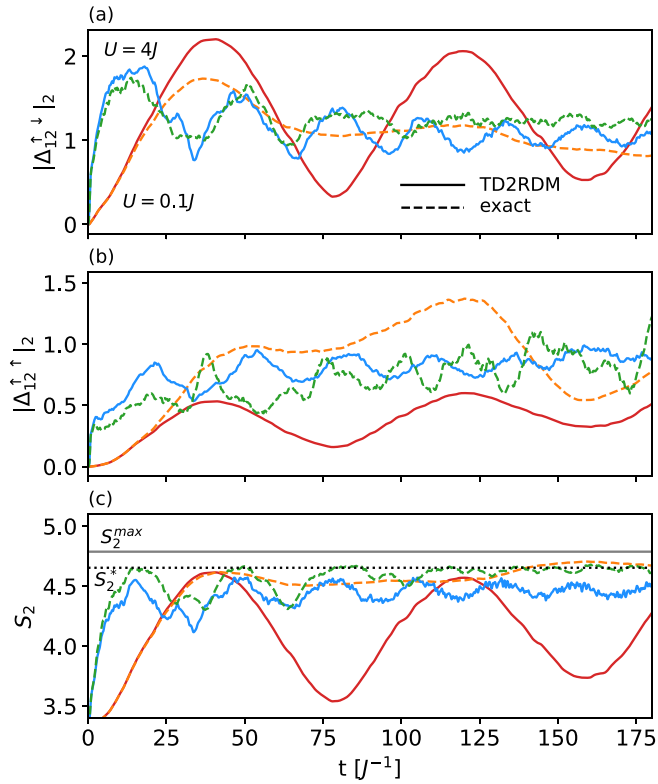

FIG. 13. Comparison between exact (dashed lines) and TD2RDM results (solid lines) for the Frobenius norm of two-particle cumulants (a) $|\Delta_{12}^{\uparrow\downarrow}|_2$ and (b) $|\Delta_{12}^{\uparrow\uparrow}|_2$ and the dynamics of the entropy S_2 (c). In (c) the solid horizontal line marks the maximal value of S_2, $S_2^{\max}$, and the dotted horizontal line denotes the value of S_2 obtained for a perfect condensate, S_2^*. Red and orange lines are for $U = 0.1J$; green and blue lines are for $U = 4J$. The system corresponds to the 1D Fermi-Hubbard model with $M_s = 8$ sites, hard wall boundary conditions, and a left aligned initial state.

fluctuating within the TD2RDM results. Overall, however, we observe good agreement up until the time scales of the order of $T_{\max}$.

APPENDIX B: CONSERVATION OF η SYMMETRY WITHIN PURIFICATION AND DETAILS ON THE NUMERICAL IMPLEMENTATION

In order to preserve N representability of the 2RDM at least partially during time propagation, we apply an *a posteriori* purification procedure after propagation time steps [30–32,38]. Without purification the TD2RDM method tends to produce 2RDMs with negative eigenvalues that ultimately may lead to instabilities [35]. Purification entails removing iteratively the defective part from the 2RDM while preserving its contraction to the 1RDM. This can be facilitated by applying the unitary decomposition of the 2RDM [37],

$$D_{12} = D_{12;\perp}\{D_1\} + D_{12;K}, \tag{B1}$$

where the kernel $D_{12;K}$ has vanishing traces, and all the trace information is contained in the orthogonal component, $D_{12,\perp}$. $D_{12,\perp}\{D_1\}$ indicates that the orthogonal component is a functional of the 1RDM. We have empirically shown [30–32]

that restoring the positive-semidefiniteness of the 2RDM and the two-hole RDM is sufficient to stabilize the equations of motion in most cases [32]. Accordingly, we determine the defective part of the 2RDM

$$D_{12}^{<} = \sum_{g_i<0} g_i |g_i\rangle\langle g_i| \tag{B2}$$

and similarly the defective part of the two-hole RDM, $Q_{12}^{<}$. Subtracting the kernel of the defective components of both the 2RDM and the two-hole RDM from the 2RDM iteratively leads to a positive semidefinite 2RDM, while preserving contraction consistency to the 1RDM. In general, however, other symmetries like, e.g., energy conservation are broken in this process unless further amendments are applied. It has been shown [38] that energy conservation can be restored by removing from $D_{12}^{<}$ and $Q_{12}^{<}$ the contributions that would lead to violations of energy conservation, before calculating the kernel. Similarly, to enforce conservation of $\langle\hat{\eta}^{+}\hat{\eta}^{-}\rangle$, Eq. (11), we set $D^{<i\uparrow i\downarrow}_{j\uparrow j\downarrow}$ and $Q^{<i\uparrow i\downarrow}_{j\uparrow j\downarrow}$ to zero for all i and j. We then determine the kernel of the correspondingly corrected defective components $D_{12}^{<}$ and $Q_{12}^{<}$ and subtract them from the 2RDM. This procedure is iteratively repeated until the required threshold for the smallest geminal occupation number is reached or until the selected maximal number of iterations is reached.

For the studies in the main text we have applied a threshold of 0 for the smallest geminal occupation number and at most 10 iteration steps within the purification for all systems except for $M_s = 60$, where only one step is applied due to its scaling with M_s^6 within the current implementation using full diagonalization of the 2RDM. Purification is applied after each global time step of $dt = 0.02J^{-1}$ within which the equations of motion, Eq. (9), are solved with adaptive time steps using a Runge-Kutta-Fehlberg propagator of fourth and fifth order. The different orders are used to adapt the time steps to achieve a prescribed accuracy. We have checked that changing the global time step to $dt = 0.01J^{-1}$, i.e., applying up to twice as many purification steps, leads to the same results to a high degree of accuracy.

APPENDIX C: FORMALISM OF EMERGENT HAMILTONIANS

We explore the applicability of the formalism of emergent Hamiltonians to the dynamical quasicondensation effect for $U < 1$. Following [28], we define a Hamiltonian $\hat{H}_0$ such that the initial state is an eigenstate of $\hat{H}_0$. One particular choice following Ref. [28] for the present initial condition is

$$\hat{H}_0 = \frac{1}{M_s}\sum_{j=1}^{M_s} j(\hat{n}_j^{\uparrow} + \hat{n}_j^{\downarrow}). \tag{C1}$$

There are, however, other possible choices such as $\hat{H}_0 = U\sum_{j=1}^{M_s}\hat{n}_j^{\uparrow}\hat{n}_j^{\downarrow}$, but they lead to essentially the same conclusions; see below. The system evolves under the influence of $\hat{H}$, Eq. (1), such that $\hat{P} = \hat{H}_0 - \hat{H}$ can be regarded as a quench. Starting from the initial condition $(\hat{H}_0 - \lambda)|\Psi(0)\rangle = 0$, one applies the time evolution operator to obtain

$$(e^{-i\hat{H}t}\hat{H}_0 e^{i\hat{H}t} - \lambda)|\Psi(t)\rangle := \hat{M}(t)|\Psi(t)\rangle. \tag{C2}$$

The operator $\hat{M}(t)$ is given by

$$\begin{aligned}\hat{M}(t) &= \hat{H} - \lambda + \hat{P} - it[\hat{H},\hat{P}] + \frac{(-it)^2}{2}[\hat{H},[\hat{H},\hat{P}]] + \cdots \\ &= \hat{H} - \lambda + \hat{P} - it\hat{Q} + \sum_{n=1}^{\infty}\frac{(-it)^{n+1}}{(n+1)!}\hat{\mathcal{H}}_n,\end{aligned} \tag{C3}$$

with the definition $\hat{Q} = [\hat{H}, P]$, and $\hat{\mathcal{H}}_n$ describing nested commutators starting with $\hat{\mathcal{H}}_1 = [\hat{H},\hat{Q}]$. According to [28] the emergent Hamiltonian is applicable if $\hat{M}(t)$ is a local operator. One particular family studied corresponds to $[\hat{H},\hat{Q}] = 0$ up to boundary terms, where the time propagated state is exponentially close to the eigenstate of the emergent Hamiltonian for times proportional to the system size [28].

For the following discussion it is convenient to separate our Hamiltonian Eq. (1) as $\hat{H} = \hat{T} + \hat{W}$, where $\hat{T}$ stands for the hopping operator proportional to J and $\hat{W}$ is the on-site interaction proportional to U. For our system with hard-wall boundary conditions (similar results hold for periodic boundary conditions) we obtain

$$\begin{aligned}\hat{Q} &= [\hat{H},\hat{P}] = [\hat{T},\hat{P}] \\ &= \frac{J}{M_s}\sum_{j=1}^{M_s-1}\sum_{\sigma}\hat{a}_{j+1\sigma}^{\dagger}\hat{a}_{j\sigma} - \frac{J}{M_s}\sum_{j=1}^{M_s-1}\sum_{\sigma}\hat{a}_{j\sigma}^{\dagger}\hat{a}_{j+1\sigma}\end{aligned} \tag{C4}$$

[note that with the prefactor $(-i)$ from Eq. (C3) this contribution to $\hat{M}(t)$ is Hermitian as it should be] and

$$\begin{aligned}\hat{\mathcal{H}}_1 &= [\hat{H},\hat{Q}] \\ &= \frac{2J^2}{M_s}(n_{M_s}^{\uparrow} + n_{M_s}^{\downarrow} - n_1^{\uparrow} - n_1^{\downarrow}) \\ &\quad + \frac{UJ}{M_s}\Bigg[\sum_{j=1}^{M_s-1}\hat{a}_{j+1\uparrow}^{\dagger}a_{j\uparrow}(\hat{n}_{j+1}^{\downarrow} - \hat{n}_j^{\downarrow}) + \text{H.c.} \\ &\quad + \sum_{j=1}^{M_s-1}\hat{a}_{j+1\downarrow}^{\dagger}a_{j\downarrow}(\hat{n}_{j+1}^{\uparrow} - \hat{n}_j^{\uparrow}) + \text{H.c.}\Bigg].\end{aligned} \tag{C5}$$

The first contribution comes from the commutator between $\hat{T}$ and $\hat{Q}$ (and corresponds to the one found in [28] for the noninteracting system), while the second term comes from the commutator between $\hat{W}$ and $\hat{Q}$. Clearly, the commutator $[\hat{H},\hat{Q}]$ does not vanish and leads to a term growing quadratically in time in $\hat{M}(t)$, Eq. (C3). Higher orders $\hat{\mathcal{H}}_n$ contain elements of the form

$$\begin{aligned}&\frac{U^n J}{M_s}\Bigg[\sum_{j=1}^{M_s-1}\hat{a}_{j+1\uparrow}^{\dagger}a_{j\uparrow}(\hat{n}_{j+1}^{\downarrow} - \hat{n}_j^{\downarrow})^n + (-1)^{n+1}\text{H.c.} \\ &\quad + \sum_{j=1}^{M_s-1}\hat{a}_{j+1\downarrow}^{\dagger}a_{j\downarrow}(\hat{n}_{j+1}^{\uparrow} - \hat{n}_j^{\uparrow})^n + (-1)^{n+1}\text{H.c.}\Bigg],\end{aligned} \tag{C6}$$

which originate from the evaluation of the n nested commutators $[\hat{W},[\hat{W},\ldots,[\hat{W},\hat{Q}]]]$. In addition, $\hat{\mathcal{H}}_n$ contains all lower orders in U, i.e., U^j with $j \in [0, n-1]$ originating from different sequences of $\hat{T}$ and $\hat{W}$ in the nested commutators and leading to products of $2(j+1)$ creation and annihilation operators. These products contain elements of the form $a_j^{\dagger}a_{j+m}$

with $m \leqslant n$ (up to $m = M_s - 1$, i.e., up to the span over the entire system). The contribution independent of U originates from repeated application of the commutator with $\hat{T}$ and contains only boundary terms. $\mathcal{M}(t)$ therefore contains arbitrarily high orders of products of creation and annihilation operators with an increasing span over the entire system, albeit being suppressed by U^m with $U < 1$ in our case and m the number of commutators containing $\hat{W}$. While the contributions from Eq. (C6) to Eq. (C3) can be evaluated to all orders leading to an extensive sum of local exponential operators, the other terms amount to an infinite series of nonlocal operators and thus cannot be easily treated. These results underline our conclusion that the present effect is not captured by an emergent Hamiltonian.

[1] A. A. Abrikosov, L. P. Gor'kov, and I. Y. Dzyaloshinskii, *Quantum Field Theoretical Methods in Statistical Physics* (Pergamon Press Ltd., Oxford, 1965).

[2] D. Fausti, R. I. Tobey, N. Dean, S. Kaiser, A. Dienst, M. C. Hoffmann, S. Pyon, T. Takayama, H. Takagi, and A. Cavalleri, Light-induced superconductivity in a stripe-ordered cuprate, Science **331**, 189 (2011).

[3] D. Nicoletti, E. Casandruc, Y. Laplace, V. Khanna, C. R. Hunt, S. Kaiser, S. S. Dhesi, G. D. Gu, J. P. Hill, and A. Cavalleri, Optically induced superconductivity in striped $La_{2-x}Ba_xCuO_4$ by polarization-selective excitation in the near infrared, Phys. Rev. B **90**, 100503(R) (2014).

[4] K. A. Cremin, J. Zhang, C. C. Homes, G. D. Gu, Z. Sun, M. M. Fogler, A. J. Millis, D. N. Basov, and R. D. Averitt, Photoenhanced metastable c-axis electrodynamics in stripe-ordered cuprate $La_{1.885}Ba_{0.115}CuO_4$, Proc. Natl. Acad. Sci. USA **116**, 19875 (2019).

[5] S. Rajasekaran, J. Okamoto, L. Mathey, M. Fechner, V. Thampy, G. D. Gu, and A. Cavalleri, Probing optically silent superfluid stripes in cuprates, Science **359**, 575 (2018).

[6] T. Suzuki, T. Someya, T. Hashimoto, S. Michimae, M. Watanabe, M. Fujisawa, T. Kanai, N. Ishii, J. Itatani, S. Kasahara, Y. Matsuda, T. Shibauchi, K. Okazaki, and S. Shin, Photoinduced possible superconducting state with long-lived disproportionate band filling in FeSe, Commun. Phys. **2**, 115 (2019).

[7] M. Mitrano, A. Cantaluppi, D. Nicoletti, S. Kaiser, A. Perucchi, S. Lupi, P. Di Pietro, D. Pontiroli, M. Riccò, S. R. Clark, D. Jaksch, and A. Cavalleri, Possible light-induced superconductivity in K_3C_{60} at high temperature, Nature (London) **530**, 461 (2016).

[8] M. Budden, T. Gebert, M. Buzzi, G. Jotzu, E. Wang, T. Matsuyama, G. Meier, Y. Laplace, D. Pontiroli, M. Riccò, F. Schlawin, D. Jaksch, and A. Cavalleri, Evidence for metastable photo-induced superconductivity in K_3C_{60}, Nat. Phys. **17**, 611 (2021).

[9] M. Buzzi, D. Nicoletti, M. Fechner, N. Tancogne-Dejean, M. A. Sentef, A. Georges, T. Biesner, E. Uykur, M. Dressel, A. Henderson, T. Siegrist, J. A. Schlueter, K. Miyagawa, K. Kanoda, M.-S. Nam, A. Ardavan, J. Coulthard, J. Tindall, F. Schlawin, D. Jaksch, and A. Cavalleri, Photomolecular high-temperature superconductivity, Phys. Rev. X **10**, 031028 (2020).

[10] J. Bloch, A. Cavalleri, V. Galitski, M. Hafezi, and A. Rubio, Strongly correlated electron–photon systems, Nature (London) **606**, 41 (2022).

[11] M. A. Sentef, A. F. Kemper, A. Georges, and C. Kollath, Theory of light-enhanced phonon-mediated superconductivity, Phys. Rev. B **93**, 144506 (2016).

[12] J. Tindall, B. Buča, J. R. Coulthard, and D. Jaksch, Heating-induced long-range η pairing in the Hubbard model, Phys. Rev. Lett. **123**, 030603 (2019).

[13] T. Kaneko, T. Shirakawa, S. Sorella, and S. Yunoki, Photoinduced η pairing in the Hubbard model, Phys. Rev. Lett. **122**, 077002 (2019).

[14] M. W. Cook and S. R. Clark, Controllable finite-momenta dynamical quasicondensation in the periodically driven one-dimensional Fermi-Hubbard model, Phys. Rev. A **101**, 033604 (2020).

[15] S. Paeckel, B. Fauseweh, A. Osterkorn, T. Köhler, D. Manske, and S. R. Manmana, Detecting superconductivity out of equilibrium, Phys. Rev. B **101**, 180507(R) (2020).

[16] M. Buzzi, G. Jotzu, A. Cavalleri, J. I. Cirac, E. A. Demler, B. I. Halperin, M. D. Lukin, T. Shi, Y. Wang, and D. Podolsky, Higgs-mediated optical amplification in a nonequilibrium superconductor, Phys. Rev. X **11**, 011055 (2021).

[17] P. E. Dolgirev, A. Zong, M. H. Michael, J. B. Curtis, D. Podolsky, A. Cavalleri, and E. Demler, Periodic dynamics in superconductors induced by an impulsive optical quench, Commun. Phys. **5**, 234 (2022).

[18] J. Hubbard, Electron correlations in narrow energy bands, Proc. R. Soc. London A **276**, 238 (1963).

[19] J. Hubbard, Electron correlations in narrow energy bands III. An improved solution, Proc. R. Soc. London A **281**, 401 (1964).

[20] M. C. Gutzwiller, Effect of correlation on the ferromagnetism of transition metals, Phys. Rev. Lett. **10**, 159 (1963).

[21] J. Kanamori, Electron correlation and ferromagnetism of transition metals, Prog. Theor. Phys. **30**, 275 (1963).

[22] M. Qin, T. Schäfer, S. Andergassen, P. Corboz, and E. Gull, The Hubbard model: A computational perspective, Annu. Rev. Condens. Matter Phys. **13**, 275 (2022).

[23] C. N. Yang, η pairing and off-diagonal long-range order in a Hubbard model, Phys. Rev. Lett. **63**, 2144 (1989).

[24] C. N. Yang, Concept of off-diagonal long-range order and the quantum phases of liquid He and of superconductors, Rev. Mod. Phys. **34**, 694 (1962).

[25] M. Rigol and A. Muramatsu, Emergence of quasicondensates of hard-core bosons at finite momentum, Phys. Rev. Lett. **93**, 230404 (2004).

[26] K. Rodriguez, S. R. Manmana, M. Rigol, R. M. Noack, and A. Muramatsu, Coherent matter waves emerging from Mott-insulators, New J. Phys. **8**, 169 (2006).

[27] L. Vidmar, J. P. Ronzheimer, M. Schreiber, S. Braun, S. S. Hodgman, S. Langer, F. Heidrich-Meisner, I. Bloch, and U. Schneider, Dynamical quasicondensation of hard-core bosons at finite momenta, Phys. Rev. Lett. **115**, 175301 (2015).

[28] L. Vidmar, D. Iyer, and M. Rigol, Emergent eigenstate solution to quantum dynamics far from equilibrium, Phys. Rev. X **7**, 021012 (2017).

[29] F. Heidrich-Meisner, M. Rigol, A. Muramatsu, A. E. Feiguin, and E. Dagotto, Ground-state reference systems for expanding correlated fermions in one dimension, Phys. Rev. A **78**, 013620 (2008).

[30] F. Lackner, I. Březinová, T. Sato, K. L. Ishikawa, and J. Burgdörfer, Propagating two-particle reduced density matrices without wave functions, Phys. Rev. A **91**, 023412 (2015).

[31] F. Lackner, I. Březinová, T. Sato, K. L. Ishikawa, and J. Burgdörfer, High-harmonic spectra from time-dependent two-particle reduced-density-matrix theory, Phys. Rev. A **95**, 033414 (2017).

[32] S. Donsa, F. Lackner, J. Burgdörfer, M. Bonitz, B. Kloss, A. Rubio, and I. Březinová, Nonequilibrium correlation dynamics in the one-dimensional Fermi-Hubbard model: A testbed for the two-particle reduced density matrix theory, Phys. Rev. Res. **5**, 033022 (2023).

[33] N. D. Mermin and H. Wagner, Absence of ferromagnetism or antiferromagnetism in one- or two-dimensional isotropic Heisenberg models, Phys. Rev. Lett. **17**, 1133 (1966).

[34] P. C. Hohenberg, Existence of long-range order in one and two dimensions, Phys. Rev. **158**, 383 (1967).

[35] A. Akbari, M. J. Hashemi, A. Rubio, R. M. Nieminen, and R. van Leeuwen, Challenges in truncating the hierarchy of time-dependent reduced density matrices equations, Phys. Rev. B **85**, 235121 (2012).

[36] N. Schlünzen, J.-P. Joost, F. Heidrich-Meisner, and M. Bonitz, Nonequilibrium dynamics in the one-dimensional Fermi-Hubbard model: Comparison of the nonequilibrium Green-functions approach and the density matrix renormalization group method, Phys. Rev. B **95**, 165139 (2017).

[37] D. A. Mazziotti, Purification of correlated reduced density matrices, Phys. Rev. E **65**, 026704 (2002).

[38] J.-P. Joost, N. Schlünzen, H. Ohldag, M. Bonitz, F. Lackner, and I. Březinová, Dynamically screened ladder approximation: Simultaneous treatment of strong electronic correlations and dynamical screening out of equilibrium, Phys. Rev. B **105**, 165155 (2022).

[39] O. Penrose and L. Onsager, Bose-Einstein condensation and liquid helium, Phys. Rev. **104**, 576 (1956).

[40] A. J. Coleman and V. I. Yukalov, *Reduced Density Matrices, Coulson's Challenge* (Springer-Verlag, Berlin, 2000).

[41] N. Gigena, M. Di Tullio, and R. Rossignoli, Many-body entanglement in fermion systems, Phys. Rev. A **103**, 052424 (2021).

[42] D. L. B. Ferreira, T. O. Maciel, R. O. Vianna, and F. Iemini, Quantum correlations, entanglement spectrum, and coherence of the two-particle reduced density matrix in the extended Hubbard model, Phys. Rev. B **105**, 115145 (2022).

[43] R. L. Stratonovich, On a method of calculating quantum distribution functions, Dokl. Akad. Nauk SSSR **115**, 1097 (1957) [Sov. Phys. Dokl., **2**, 416 (1957)].

[44] J. Hubbard, Calculation of partition functions, Phys. Rev. Lett. **3**, 77 (1959).

[45] J. W. Negele and H. Orland, *Quantum Many-Particle Systems* (Addison-Wesley Publishing Company, Redwood City, CA, 1988).

[46] L. W. Cheuk, M. A. Nichols, M. Okan, T. Gersdorf, V. V. Ramasesh, W. S. Bakr, T. Lompe, and M. W. Zwierlein, Quantum-gas microscope for fermionic atoms, Phys. Rev. Lett. **114**, 193001 (2015).

[47] M. F. Parsons, F. Huber, A. Mazurenko, C. S. Chiu, W. Setiawan, K. Wooley-Brown, S. Blatt, and M. Greiner, Site-resolved imaging of fermionic ^{6}Li in an optical lattice, Phys. Rev. Lett. **114**, 213002 (2015).

[48] E. Haller, J. Hudson, A. Kelly, D. A. Cotta, B. Peaudecerf, G. D. Bruce, and S. Kuhr, Single-atom imaging of fermions in a quantum-gas microscope, Nat. Phys. **11**, 738 (2015).

[49] G. J. A. Edge, R. Anderson, D. Jervis, D. C. McKay, R. Day, S. Trotzky, and J. H. Thywissen, Imaging and addressing of individual fermionic atoms in an optical lattice, Phys. Rev. A **92**, 063406 (2015).

[50] A. Omran, M. Boll, T. A. Hilker, K. Kleinlein, G. Salomon, I. Bloch, and C. Gross, Microscopic observation of pauli blocking in degenerate fermionic lattice gases, Phys. Rev. Lett. **115**, 263001 (2015).

[51] Y. Cai, D. G. Allman, P. Sabharwal, and K. C. Wright, Persistent currents in rings of ultracold fermionic atoms, Phys. Rev. Lett. **128**, 150401 (2022).

[52] L. Balents, C. R. Dean, D. K. Efetov, and A. F. Young, Superconductivity and strong correlations in moiré flat bands, Nat. Phys. **16**, 725 (2020).

[53] A. O. Schouten, L. A. M. Sager-Smith, and D. A. Mazziotti, Large cumulant eigenvalue as a signature of exciton condensation, Phys. Rev. B **105**, 245151 (2022).

[54] D. A. Mazziotti, Approximate solution for electron correlation through the use of Schwinger probes, Chem. Phys. Lett. **289**, 419 (1998).

[55] I. Absar and A. Coleman, One electron orbitals intrinsic to the reduced Hamiltonian, Chem. Phys. Lett. **39**, 609 (1976).

[56] J. E. Harriman, Geometry of density matrices. II. Reduced density matrices and n-representability, Phys. Rev. A **17**, 1257 (1978).

[57] F. Colmenero, C. Pérez del Valle, and C. Valdemoro, Approximating q-order reduced density matrices in terms of the lower-order ones. I. General relations, Phys. Rev. A **47**, 971 (1993).

[58] K. Yasuda and H. Nakatsuji, Direct determination of the quantum-mechanical density matrix using the density equation. II, Phys. Rev. A **56**, 2648 (1997).